

## A Quantitative Curve-Crossing Model for Radical Fragmentation

Edward D. Lorance

Department of Chemistry, Vanguard University, Costa Mesa, California 92626

Ian R. Gould\*

Department of Chemistry and Biochemistry, Arizona State University, Tempe, Arizona 85287-1604

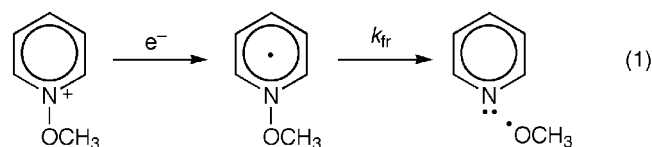
Received: November 3, 2004; In Final Form: January 17, 2005

The kinetics of bond fragmentation for a series of *N*-methoxyppyridyl radicals are analyzed in terms of a simple curve-crossing model that includes bond stretching and bond bending coordinates. The model accurately reproduces the reaction surfaces calculated using density functional theory (DFT) and also the experimental reaction energy barriers. The reactions proceed on the ground state surface by avoidance of a conical intersection, which is clearly illustrated by the model. A value for the electronic coupling matrix element responsible for splitting the upper and lower surfaces of 0.9 eV is obtained. The model illustrates the molecular features that allow barrierless fragmentation from a formally  $\pi^*$  radical.

### Introduction

Transition state theory remains the most widely used method for the analysis of reaction rate constants in organic chemistry.<sup>1,2</sup> Although transition state theory successfully relates the rate of a reaction to its barrier height, it does not describe the factors that control the height of the barrier nor allow predictions of how to make the barrier larger or smaller. Curve-crossing models relate barrier height to the overall reaction energy change and form the basis of many other theoretical descriptions of chemical reaction kinetics, including the Bell–Evans–Polyani principle,<sup>3</sup> the Hammond postulate,<sup>4</sup> Marcus theory,<sup>5</sup> the Shaik/Pross VBCM model,<sup>6</sup> and Saveant's description of reductive cleavage reactions.<sup>7</sup> In principle, parametrization of such a theory could allow reaction barrier heights, and hence rate constants, to be predicted, although examples of this are rare.<sup>6,8–10</sup>

In a recent series of papers, we have described the kinetics of N–O bond fragmentation in a series of *N*-methoxyppyridyl radicals formed by one-electron reduction of the corresponding pyridiniums, as illustrated in eq 1 for the parent system.<sup>11</sup> These reactions are of interest for several reasons.



First, their reaction path is determined by avoidance of a conical intersection.<sup>11</sup> The importance of conical intersections in photochemical processes is well-known,<sup>12</sup> but their role in ground state reactions is less frequently discussed.<sup>10,13</sup> Second, avoided crossings around conical intersections involve the mixing of ground and excited states characterized by intramolecular electron and energy transfer matrix elements. Evaluation of such matrix elements is central to research on radiationless and radiative transitions.<sup>14,15</sup> With the exception of the VCBM model of Shaik and Pross,<sup>6</sup> however, discussion of their role in ground state chemical reactions is less common,<sup>10,15a,16</sup> in part, because their values are difficult to determine. Finally, some

of the *N*-methoxyppyridyl radicals studied previously underwent bond fragmentation apparently with little or no barrier to reaction.<sup>11b,c</sup> The design of electron transfer activated bond fragmentation reactions that occur at the highest possible rate has been the subject of considerable research over many years,<sup>17</sup> yet very few definitive examples of such reactions that occur with no barrier have been reported.

Previously, we found that a qualitative curve-crossing model provided a useful understanding of the rates of these reactions.<sup>11</sup> The model accounted for substituent effects and was found to be predictive in terms of relative reactivity. We wondered whether a quantitative curve-crossing model could simulate the absolute rate constants for the reactions.

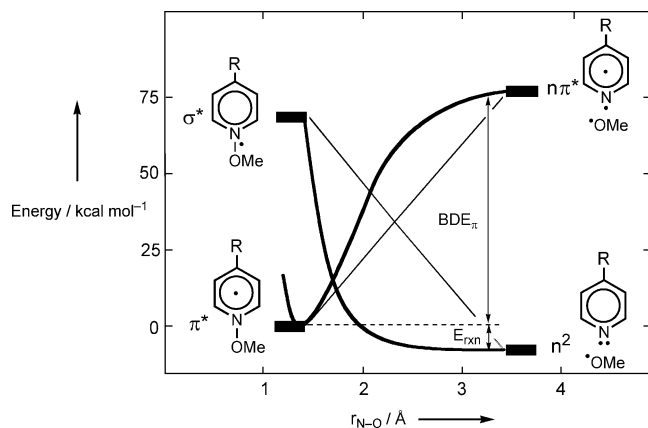
Proper description of the fragmentation reaction of *N*-methoxyppyridyl radicals requires the consideration of two important coordinates, that is, bond stretching and out-of-ring plane bond bending.<sup>11</sup> Hynes et al. recently described in detail a quantitative 3-D curve-crossing model for a closely related reaction, that is, fragmentation of the radical anion of the *p*-cyanophenyl chloride radical anion, as a function of the same two coordinates.<sup>10</sup> The Hynes model included a detailed description of solvation effects and used modified transition state theory to successfully simulate the kinetics of the C–Cl bond fragmentation process. Importantly, the matrix element responsible for splitting of the ground and excited radical anion (diabatic) states was also obtained.<sup>10</sup>

Herein, we describe a quantitative model for the pyridyl radical fragmentation reaction of the “Hynes” type,<sup>10</sup> that accurately reproduces the reaction barriers for a series of fragmentation reactions with a wide range in rate constants. The model is extremely simple to implement and, in addition to reaction barriers, provides structural information for both the radical minima and transition states. The model clearly illustrates the factors that control the relative reaction barrier heights for the reactions, and the origin of a barrierless reaction is easily understood.

### Development of the Model

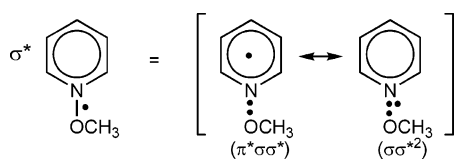
Reduction of an *N*-methoxyppyridinium puts the extra electron into a  $\pi^*$  orbital associated with the aromatic ring. This  $\pi^*$  state

\* Corresponding author. E-mail: igould@asu.edu.



**Figure 1.** Energy correlation diagram for a  $\pi^*$  pyridyl radical (bottom left) and  $\sigma^*$  radical (top left) as a function of N–O bond length,  $r_{\text{N-O}}$ . The solid lines show the correlations for the planar radicals. The curves show the Morse energy curve for the  $\pi^*$  radical and the repulsive energy curve for the  $\sigma^*$  radical calculated using eq 2, with the parameters given in Table 1, and a reaction exothermicity,  $E_{\text{rxn}}$ , of 6.4 kcal/mol.

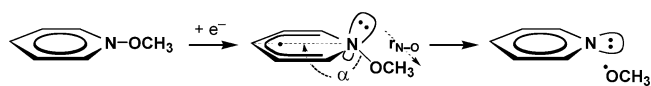
### SCHEME 1



is stable with respect to dissociation of the N–O bond, since the  $\sigma$  bond order remains unaffected. As shown by the straight-line correlation in Figure 1, stretching the N–O bond in this radical yields the methoxy radical and pyridine with one electron in the  $\pi^*$  orbital and one in a nonbonding orbital on nitrogen, that is, a pyridine  $n \rightarrow \pi^*$  excited state ( $n\pi^*$  in Figure 1). Formation of the ground state pyridine and methoxy radical products ( $n^2$  in Figure 1) thus requires the participation of  $\sigma^*$  excited states of the radical. In this regard, the aryl halide radical anion<sup>7,10</sup> and pyridyl radical systems are slightly different. In the halides, the presence of an electron in the  $\sigma^*$  orbital results in a three-electron C–Cl bond that may be repulsive and lead to the product aryl anion and halide anion directly.<sup>18</sup> Because of the smaller difference in electronegativity, however, the N–O three-electron bond may not be repulsive, and higher excited  $\sigma^*$  states are probably involved.<sup>11b,c</sup> Two states that were discussed previously are illustrated in Scheme 1. One of these has one electron in each of the  $\pi^*$ ,  $\sigma$ , and  $\sigma^*$  orbitals ( $\pi\sigma\sigma^*$ ), and another has one in the  $\sigma$  orbital and two in the  $\sigma^*$  orbital ( $\sigma\sigma^{*2}$ ) (Scheme 1). These ( $\pi\sigma\sigma^*$ ) and ( $\sigma\sigma^{*2}$ ) states readily mix upon out-of-ring plane bending of the N–O bond. The nature of the mixed state depends on the N–O bond length. At short bond lengths, the ( $\pi\sigma\sigma^*$ ) state is lower in energy and the mixed state has mainly this character. At longer bond lengths, the repulsive ( $\sigma\sigma^{*2}$ ) state dominates and yields the ground state pyridine and methoxy radical products at large separation. To simplify the model, we assume a single mixed  $\sigma^*$  state (Figure 1) that changes character smoothly with increasing N–O bond distance and correlates with the ground product state  $n^2$  in Figure 1.

The reaction is thus characterized by a crossing of the  $\pi^*$  (attractive) and  $\sigma^*$  (repulsive) excited states. A critical point is that mixing of the  $\pi^*$  and  $\sigma^*$  states is symmetry forbidden in the planar radical and an avoided crossing only occurs when the N–O bond is bent out of the ring plane.<sup>10,11</sup> The curve-crossing model is thus properly defined in terms of two

### SCHEME 2



coordinates, that is, N–O bond stretching,  $r_{\text{N-O}}$ , and bending,  $\alpha$  (Scheme 2).

The energy difference between the  $\pi^*$  and  $n\pi^*$  states of Figure 1 is the N–O bond dissociation energy ( $\text{BDE}_{\pi}$ ) of the planar  $\pi^*$  radical.<sup>8b</sup> The energy difference between the product  $n^2$  state and the  $n\pi^*$  state, the pyridine excited state energy, is thus equal to the sum of  $\text{BDE}_{\pi}$  and  $E_{\text{rxn}}$ , the reaction exothermicity (Figure 1).

The energy difference between the product  $n^2$  and the  $\sigma^*$  state is less well-defined. In previous curve-crossing models of this type, however,<sup>8b,10</sup> this energy difference has been equated to  $\text{BDE}_{\pi}$ . We have made the same assumption here, although we have also sought some independent justification. First, the energy difference between the  $\pi^*$  state and a pure ( $\pi\sigma\sigma^*$ ) state is roughly equal to the bond dissociation energy, since this is the energy required to transfer an electron from the  $\sigma$  orbital to the  $\sigma^*$  orbital.<sup>6</sup> The energy difference between the  $\pi^*$  and  $\sigma^*$  states in Figure 1 is thus somewhat less than  $\text{BDE}_{\pi}$ , due to mixing of the ( $\pi\sigma\sigma^*$ ) and ( $\sigma\sigma^{*2}$ ) states. If the decrease in energy due to mixing is of the same order as  $E_{\text{rxn}}$ , then the assumption is accurate. This assumption has also been tested using a time-dependent density functional theory (DFT) computation; see further below.

Construction of the model starts with a more realistic description of the N–O bond stretching coordinate than the straight-line correlations of Figure 1. The energy of the bound  $\pi^*$  configuration as a function of N–O distance,  $E_{\pi}(r)$ , can be given in terms of a Morse potential (eq 2a)<sup>8b</sup> where the value of the curve at infinite bond length equals  $\text{BDE}_{\pi}$ ,  $\beta$  is the asymmetry parameter, and zero energy is defined to be the bottom of the Morse curve. The energy of the  $\sigma^*$  configuration,  $E_{\sigma}(r)$ , can be described as the repulsive component of the Morse curve (eq 2b).<sup>8b,10</sup> The energies are given in terms of  $\Delta r_{\text{N-O}}$ , the difference between the actual bond length,  $r_{\text{N-O}}$ , and that of the  $\pi^*$  radical configuration at its minimum energy,

$$E_{\pi}(r) = \text{BDE}_{\pi}(1 + \exp(-2\beta\Delta r_{\text{N-O}}) - 2 \exp(-\beta\Delta r_{\text{N-O}})) \quad (2a)$$

$$E_{\sigma}(r) = (\text{BDE}_{\pi} \exp(-2\beta\Delta r_{\text{N-O}})) - E_{\text{rxn}} \quad (2b)$$

$r_{\text{min}}$ . Examples of these potential energy curves are shown superimposed on the straight-line correlations in Figure 1.

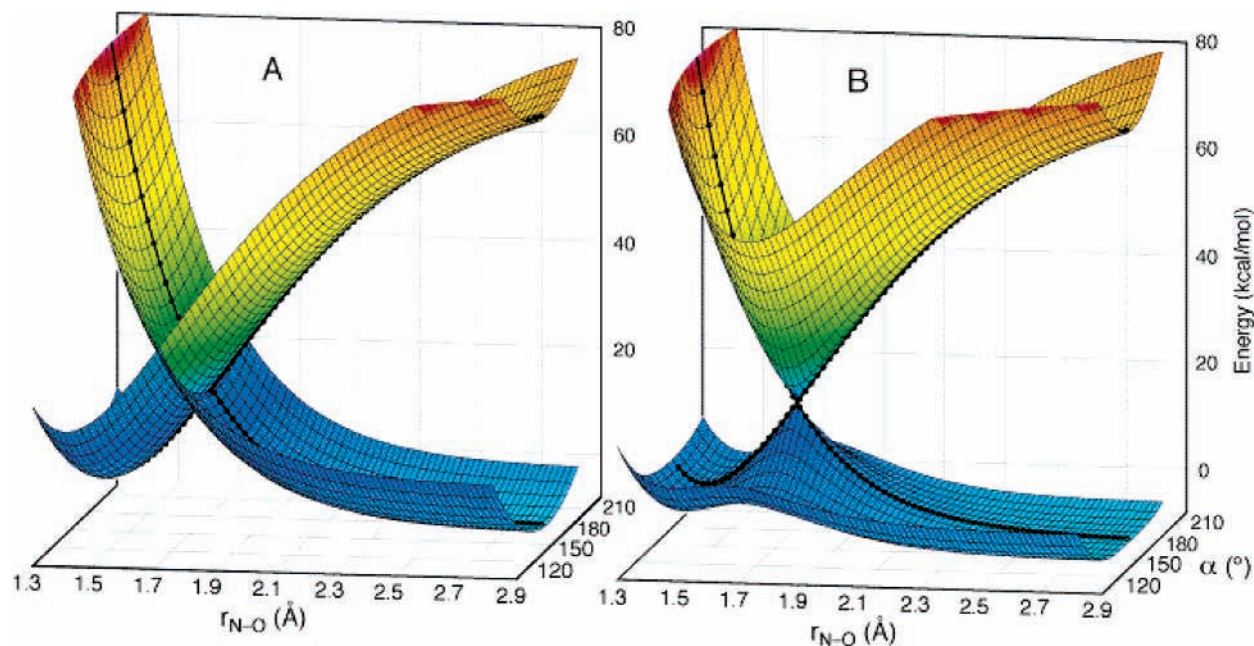
The energy of the diabats in the second (bending) coordinate is estimated as a standard bending potential,  $E_{\text{bend}}$ . These can take complex forms, but a simple quadratic potential works well (eq 3).<sup>19</sup> Here,  $k_{\text{bend}}$  is the out-of-plane bending force constant and  $\alpha$  is the bend angle in radians. The bending potential is

$$E_{\text{bend}} = k_{\text{bend}}(\pi - \alpha)^2 \quad (3)$$

included in the model by simple addition to the bond stretch potentials to give the diabatic energies as a function of  $r_{\text{N-O}}$  and  $\alpha$ ,  $D_{\pi}(r, \alpha)$ , and  $D_{\sigma}(r, \alpha)$  (eq 4). Examples of these diabats are illustrated in Figure 2A. The bending potential is assumed to be

$$D_{\pi}(r, \alpha) = E_{\pi}(r) + E_{\text{bend}}(\alpha) \quad (4a)$$

$$D_{\sigma}(r, \alpha) = E_{\sigma}(r) + E_{\text{bend}}(\alpha) \quad (4b)$$



**Figure 2.** (A) Diabatic  $\pi^*$  and  $\sigma^*$  surfaces as a function of N–O distance,  $r_{\text{N-O}}$ , and out-of-plane bending angle,  $\alpha$ . (B) Lower reactive (mainly blue) and upper excited (yellow/green) adiabatic surfaces formed by mixing the diabatic surfaces from part A. The Morse and repulsive curves from which the diabatic and adiabatic surfaces are derived are indicated by the black dots in each part of the figure. The surfaces are calculated using the parameters of Table 1 and for a reaction exothermicity of 6.4 kcal/mol.

the same for both diabats and to be independent of  $r_{\text{N-O}}$ . Bending is associated with rehybridization of the nitrogen and in the absence of mixing results in an increase in energy because (in addition to other electron repulsion effects) two electrons formally associated with nitrogen occupy a nonbonding atomic orbital on nitrogen when bent but occupy lower energy  $\pi$  bonding orbitals on the ring when planar. This is the case whether there is actually an N–O bond or not; hence, the assumption that bending is independent of  $r_{\text{N-O}}$  seems safe.

The adiabatic reaction surface is formed using a simple two-state perturbation model, which gives the relationship between the diabatic and adiabatic state energies, as shown in eq 5a.

$$\begin{vmatrix} (D_\pi - E) & V \\ V & (D_\sigma - E) \end{vmatrix} = 0 \quad (5a)$$

$$E_{u,l} = \frac{D_\pi + D_\sigma \pm \sqrt{(D_\pi + D_\sigma)^2 - 4(D_\pi D_\sigma - V^2)}}{2} \quad (5b)$$

Here,  $V$  is the matrix coupling element and  $E$  is the adiabatic energy, which has two values,  $E_u$  and  $E_l$ , for any given set of the independent variables that determine  $D_\pi$  and  $D_\sigma$ . Solving for these values using eq 5b yields the energy of the lower reaction adiabatic potential energy surface,  $E_l$ , and an excited upper adiabatic surface,  $E_u$ . The matrix coupling element,  $V$ , is related to the orbital overlap between the  $\pi$  and  $\sigma$  radical states. We have approximated this overlap using a sine function (eq 6) where  $V_{\text{max}}$  is the coupling at maximum orbital overlap. Using eqs 2–6,

$$V = V_{\text{max}} \sin(\pi - \alpha) \quad (6)$$

values for  $E_l$  and  $E_u$  as a function of  $r_{\text{N-O}}$  and  $\alpha$  are easily computed, and examples are given in Figure 2B. The reactive lower and excited upper surfaces exhibit extensive splitting, except at the crossing point in the planar conformation, where they meet at a conical intersection. Under transition state theory

**TABLE 1: Values of Fitting Parameters That Give the Best Fit to B3PW91/6-31+G\* Computed Potential Energy Curves for Fragmentation of the *N*-Methoxyphenyl Radicals of Table 2<sup>a</sup>**

$\text{BDE}_\pi$ (kcal mol <sup>-1</sup> )	$\beta$ (Å <sup>-1</sup> )	$r_{\text{min}}$ (Å)	$k_{\text{bend}}$ (kcal mol <sup>-1</sup> rad <sup>-2</sup> )	$V_{\text{max}}$ (kcal mol <sup>-1</sup> )
76.7	2.11	1.40	4.9	20.8


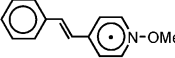

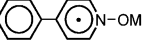
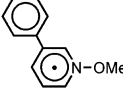
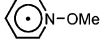

<sup>a</sup> See text for definition of symbols.

assumptions, the reactions proceed via the minimum energy geometry at the transition state, avoiding the conical intersection.

N–O bond fragmentation in the series of pyridyl radicals indicated in Table 2 has been studied previously using hybrid density functional computations (B3PW91/6-31+G\*).<sup>11c</sup> A best fit to these DFT potential energy surfaces for radicals 1–7 was obtained using the curve-crossing model (eqs 2–6). The parameters  $\text{BDE}_\pi$ ,  $\beta$ ,  $r_{\text{min}}$ ,  $k_{\text{bend}}$ , and  $V$  were varied globally (that is, they were set to the same for every compound).  $E_{\text{rxn}}$ , the reaction exothermicity, is the parameter that distinguishes the various reactions and was allowed to vary for each radical. A final parameter,  $E_{\text{off}}$ , is a compound-dependent shift parameter, expected and found to be small, which reflects the fact that the DFT energies are normalized to those at the minimum geometries. These geometries are not that of the pure  $\pi^*$  state minimum, that is, at  $r_{\text{N-O}} = r_{\text{min}}$ , the energy upon which the calculated surfaces were based. The offsets should be dependent on the reaction exothermicity, and this was found to be the case (Table 2). Because the model describes the best fit to DFT computed energy surfaces,  $E_{\text{rxn}}$  and  $E_{\text{off}}$  are electronic energies. The parameters that best fit the DFT data are those summarized in Tables 1 and 2. The *p*-styrylpyridyl radical, 2, has a reaction exothermicity of 6.4 kcal/mol; thus, Figures 1 and 2 describe the diabatic and adiabatic energy curves and surfaces for this particular reaction.

The fits to the DFT surfaces are illustrated in Figure 3 for several of the radicals. For each radical, a contour plot is shown of energy versus angle versus  $r_{\text{N-O}}$ , calculated using the curve-

**TABLE 2: Model Parameters,  $E_{\text{rxn}}$  and  $E_{\text{off}}$ , Calculated Model Activation Free Energies,  $\Delta G^{\ddagger}_{\text{calc}}$ , DFT Computed Activation Free Energies,  $\Delta G^{\ddagger}_{\text{DFT}}$ , and Experimental Activation Free Energies,  $\Delta G^{\ddagger}_{\text{expt}}$ , for N–O Bond Fragmentation in *N*-Methoxypyridyl Radicals**

Structure	Radical	$E_{\text{rxn}}^a$ kcal mol <sup>-1</sup>	$E_{\text{off}}^b$ kcal mol <sup>-1</sup>	$\Delta G^{\ddagger}_{\text{Calc}}^c$ kcal mol <sup>-1</sup>	$\Delta G^{\ddagger}_{\text{DFT}}^d$ kcal mol <sup>-1</sup>	$\Delta G^{\ddagger}_{\text{Exp}}^e$ kcal mol <sup>-1</sup>
	<b>1</b>	-2.34	-0.15	6.59	7.29	f
	<b>2</b>	6.39	-0.37	2.75	2.71	4.27
	<b>3</b>	5.44	-0.35	3.12	3.10	3.72
	<b>4</b>	12.26	-0.64	0.79	0.70	1.87
	<b>5</b>	15.71	-0.95	-0.09	-0.22	1.19
	<b>6</b>	15.42	-1.0	-0.02	-0.22	0.80
	<b>7</b>	23.24 <sup>g</sup>	-2.0	-1.83 <sup>g</sup>	-2.15 <sup>g</sup>	f

<sup>a</sup> Model electronic reaction energy, see text. <sup>b</sup> Model electronic energy offset parameter, see text. <sup>c</sup> Calculated using eq 7 as described in the text. <sup>d</sup> B3PW91/6-31+G\* computed activation free energy.<sup>11c</sup> <sup>e</sup> Experimental activation energy.<sup>11a,b</sup> <sup>f</sup> Not measured. <sup>g</sup> Average of energies at 1.4 and 1.5 Å for the minimum and 1.5 and 1.6 Å for the transition state, since no barrier was found.<sup>11c</sup>

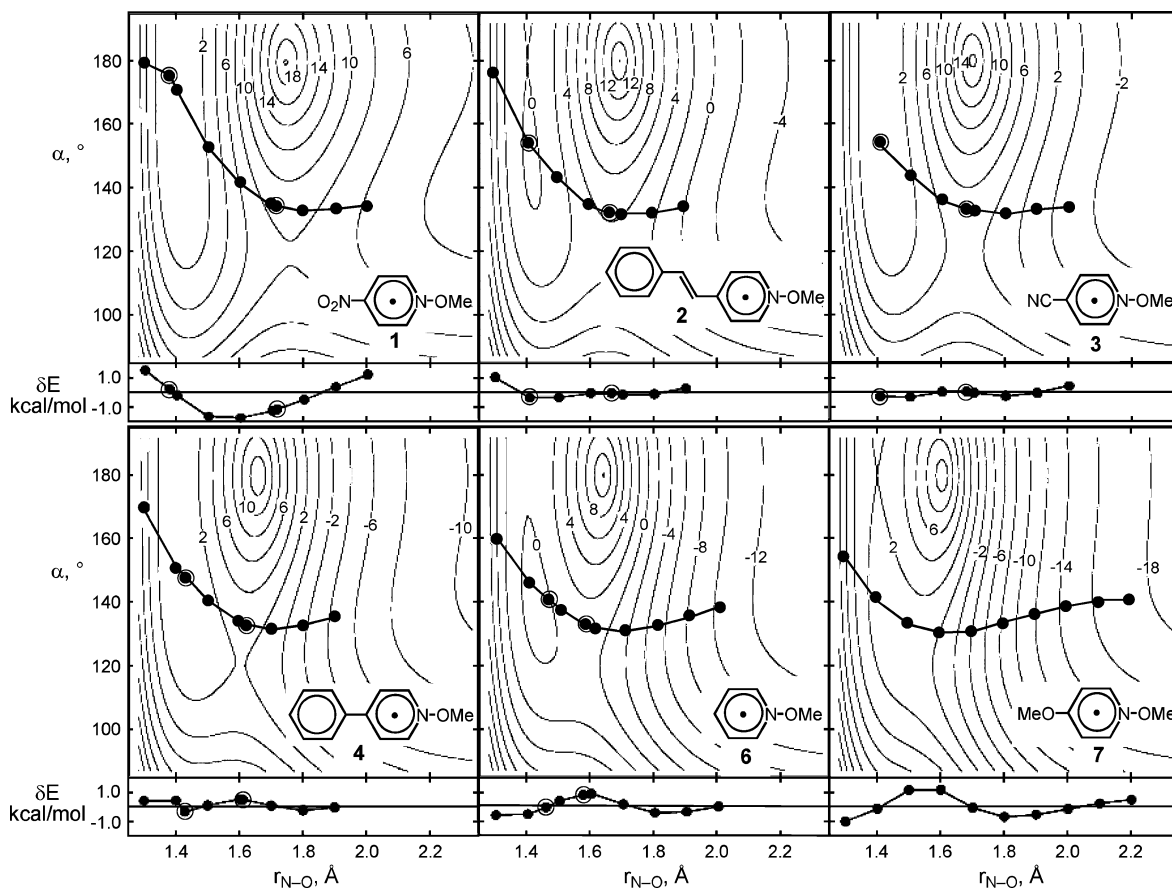
crossing model. The points on the contour plots indicate the DFT computed angles versus  $r_{\text{N-O}}$  for each reaction. Below each contour plot is shown the difference between the DFT and the calculated energies at each  $r_{\text{N-O}}$ . The fitting routine determined the values of the global ( $\text{BDE}_{\pi}$ ,  $\beta$ ,  $r_{\text{min}}$ ,  $k_{\text{bend}}$ , and  $V$ ) and reaction specific ( $E_{\text{rxn}}$  and  $E_{\text{off}}$ ) parameters that best reproduced the DFT energies at each  $r_{\text{N-O}}$  for each reaction. Reproduction of the DFT bending angles was not included as part of the fitting routine, and the angles obtained from the model are simply those that give the best fits to the DFT energies. Nevertheless, the DFT angles are reproduced reasonably well by the model, as illustrated by the fact that the points lie close to the lowest energy path for each reaction predicted by the model. The angles at the transition states are somewhat overestimated by the model, particularly for radical **1**, and indeed, the fit to the DFT energy profile for this radical is the worst of all of the reactions. However, the maximum deviation between the model and DFT energies for this reaction is 1.7 kcal/mol, which corresponds to only 6% of the total range of DFT energies included in the fitting procedure. Most of the differences between the model and the DFT energies are considerably <1 kcal/mol, that is, <3.5% of the total range of DFT energies.

As discussed above, the reactions proceed via avoidance of a conical intersection,<sup>10,11</sup> and this feature is clearly illustrated in the contour plots of Figure 3. In each reaction, the radical has to undergo considerable N–O bending to get “around” the high-energy cone and then traverse the transition state mainly along the N–O stretching coordinate.

The bond dissociation energy and length parameters obtained,  $\text{BDE}_{\pi}$  and  $r_{\text{min}}$ , correspond to the pure  $\pi^*$  diabatic planar radical. The DFT computed minimum N–O bond lengths for the actual radicals used in the fitting, **3–7**, range from 1.41 to 1.46 Å (Table 3). As discussed further below, these should all be longer than that for the pure  $\pi^*$  radical, as they were found to be. The computed value for the *p*-nitro radical, **1**, is somewhat shorter than  $r_{\text{min}}$  but only by 0.02 Å.

The model assumes that the energy difference between the diabatic  $n^2$  and  $\sigma^*$  states (connected by the repulsive curve in Figure 1) is equal to  $\text{BDE}_{\pi}$ . The  $\sigma^*$  state in Figure 1 is an excited state of the  $\pi^*$  radical in the absence of mixing, that is, when the out-of-plane bending angle,  $\alpha$  (Scheme 2), is zero. According to Figure 1, the difference in energy between the pure  $\pi^*$  and  $\sigma^*$  states at small N–O should be equal to  $\text{BDE}_{\pi}$  minus the reaction exothermicity,  $E_{\text{rxn}}$ . A time-dependent DFT computation was performed on the parent pyridyl radical in an attempt to determine the actual energy difference between the  $\pi^*$  and  $\sigma^*$  states. The equilibrium geometry of the pyridyl radical is quite bent ( $\alpha = 141^\circ$ ).<sup>11c</sup> The computation, however, was performed with the N–O bond length fixed at 1.4 Å (i.e., the bond length for the pure  $\pi^*$  radical obtained from the simulations, Table 1) and the angle  $\alpha$  fixed at  $180^\circ$ , to eliminate mixing between the  $\pi^*$  and  $\sigma^*$  states.

Five excited states were obtained, with (electronic) energies above the ground state of 32.7, 62.8, 72.8, 75.9, and 76.3 kcal/mol (see the Experimental Section). Of these, the lowest energy transition is clearly  $\pi - \pi^*$ , but the second, with an energy of 62.8 kcal/mol, was found to have mainly  $\pi - \sigma^*$  character, which we assign to the vertical excitation shown in Figure 1. For the parent pyridyl radical, the reaction exothermicity is 15.4 kcal/mol (Table 2). Thus, together with a  $\text{BDE}_{\pi}$  of 76.7 kcal/mol (Table 1), the model predicts an energy difference between pure  $\pi^*$  and  $\sigma^*$  states at 1.4 Å of 61.3 kcal/mol. This is in remarkably good agreement with the 62.8 kcal/mol value from the time-dependent DFT computation, in support of both the assumption of the  $n^2 - \sigma^*$  energy gap in Figure 1 and the model in general. As a further test of the assumption, and of the interrelationship between the parameters, we have examined the effect of allowing the energy gap between the  $n^2$  and  $\sigma^*$  states to be different from  $\text{BDE}_{\pi}$ . We find that allowing these energies to differ by up to 10 kcal/mol results in changes in the optimized values for most of the other parameters of <10%. Details are given in the Supporting Information.



**Figure 3.** Contour plots of energy (kcal/mol) versus N–O distance,  $r_{\text{N-O}}$ , versus out-of-plane bending angle,  $\alpha$ , calculated using eqs 2–6 and the parameters in Tables 1 and 2, for the radicals shown. The points indicate DFT angles versus  $r_{\text{N-O}}$  for the reactions from ref 11c; the circled points represent the radical minima and transition states. There are no minimum or transition state for **7** because this reaction has no barrier. Also shown are the energy differences,  $\delta E$ , between those calculated using the model and those computed using DFT, as a function of  $r_{\text{N-O}}$ . The plots for radical **5** are not shown; they are very similar to those for radical **6**.

**TABLE 3: Geometrical Parameters from the Model Compared to Those Computed by DFT for N–O Bond Fragmentation in N-Methoxyppyridyl Radicals**

radical	$r_{\text{min}}^{\text{DFT } a}$ (Å)	$r_{\text{min}}^{\text{calcd } b}$ (Å)	$\alpha_{\text{min}}^{\text{DFT } a}$ (deg)	$\alpha_{\text{min}}^{\text{calcd } b}$ (deg)	$r_{\ddagger}^{\text{DFT } a}$ (Å)	$r_{\ddagger}^{\text{calcd } b}$ (Å)	$\alpha_{\ddagger}^{\text{DFT } a}$ (deg)	$\alpha_{\ddagger}^{\text{calcd } b}$ (deg)
<b>1</b>	1.38	1.41	175	157	1.71	1.76	134	120
<b>2</b>	1.41	1.42	154	147	1.67	1.67	132	120
<b>3</b>	1.41	1.41	155	149	1.68	1.67	133	120
<b>4</b>	1.43	1.42	147	141	1.61	1.60	133	121
<b>5</b>	1.46	1.43	142	137	1.57	1.57	134	122
<b>6</b>	1.46	1.43	141	137	1.58	1.57	134	124
<b>7</b>	1.45 <sup>c</sup>	1.45 <sup>c</sup>	136 <sup>c</sup>	132 <sup>c</sup>	1.55 <sup>c</sup>	1.55 <sup>c</sup>	131 <sup>c</sup>	121 <sup>c</sup>

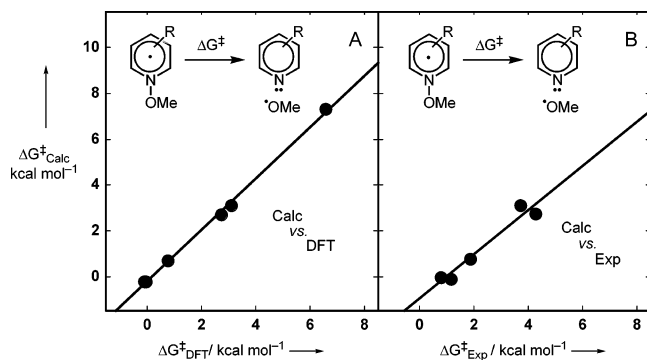
<sup>a</sup> B3PW91/6-31+G\* computed bond lengths and bend angles at the radical minima (min) and transition states ( $\ddagger$ ).<sup>11c</sup> <sup>b</sup> Bond lengths and angles from the model, using eqs 2–6 and the parameters given in Tables 1 and 2, at the radical minima (min) and transition states ( $\ddagger$ ). <sup>c</sup> These values refer to an average of those determined at 1.4 and 1.5 Å for the minimum and 1.5 and 1.6 Å for the transition state, since no barrier was found in this case.<sup>11c</sup>

A bending coefficient of 4.9 kcal/mol·radians<sup>2</sup> was determined. As discussed above, in essence, this corresponds to a rehybridization coefficient. Although there are several differences between the N–O bond breaking reaction studied here and the C–Cl bond breaking reaction studied by Hynes et al.,<sup>10</sup> our value is comparable to the value 11.5 kcal/mol·radians<sup>2</sup> determined for the *p*-cyanophenyl chloride radical anion (when differences in the formulation of the respective equations are taken into account).<sup>10a</sup> It is reasonable that the coefficient is larger for the aryl chloride radical anion, since rehybridization localizes a pair of electrons on carbon in this case, compared to corresponding lone pair localization on nitrogen in the pyridyl radical reaction. The more electronegative nitrogen can more easily accommodate these electrons and thus rehybridizes more easily.

The crucial parameter is the matrix coupling element that determines the extent of  $\pi^*/\sigma^*$  mixing. The optimal value for  $V_{\text{max}}$  was found to be 0.9 eV (20.8 kcal/mol), which yields a splitting between the adiabatic states at the transition states of 38–41 kcal/mol, depending upon the particular reaction. This can be compared to the value that Hynes et al. found for the *p*-cyanophenyl chloride radical anion of 0.62 kcal/mol·degree (for a linear dependence of  $V$  on the hybridization angle), yielding a coupling coefficient of 16.12 kcal/mol at the transition state (or an approximate splitting of 32 kcal/mol).<sup>10</sup>

### The N–O Bond Fragmentation Reaction

Reaction barriers can be determined from the curve-crossing model as the energy difference between the radical minima and



**Figure 4.** Activation free energies for N–O bond fragmentation in *N*-methoxyppyridyl radicals from the curve-crossing model,  $\Delta G_{\text{calc}}^{\ddagger}$ , versus (A) DFT computed free energies (slope 1.12, intercept  $-0.23$ ) and (B) experimental reaction free energies (slope 0.96, intercept  $-0.97$ ).

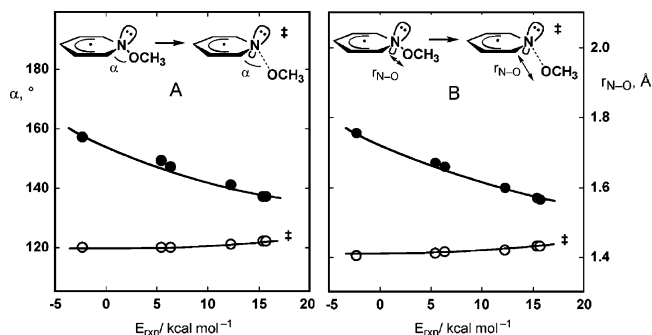
transition states. Because the model is parametrized using DFT electronic energies, this is an electronic energy difference,  $\Delta E_{\text{calc}}^{\ddagger}$ .<sup>20</sup> However, the previously determined DFT activation free energies,  $\Delta G_{\text{DFT}}^{\ddagger}$ , exhibit an excellent linear correlation with the corresponding DFT electronic energy differences,  $\Delta E_{\text{DFT}}^{\ddagger}$ , according to eq 7.<sup>10c</sup> Therefore, we can calculate activation free energies given by the model,  $\Delta G_{\text{calc}}^{\ddagger}$ , by

$$\Delta G_{\text{DFT}}^{\ddagger} = 0.96\Delta E_{\text{DFT}}^{\ddagger} - 0.92 \quad (7)$$

assuming the relationship of eq 7 holds also for  $\Delta E_{\text{calc}}^{\ddagger}$  from the model. The  $\Delta G_{\text{calc}}^{\ddagger}$  values obtained in this way are summarized in Table 2 and are compared to the corresponding DFT values,  $\Delta G_{\text{DFT}}^{\ddagger}$ , and also those from experiment,  $\Delta G_{\text{expt}}^{\ddagger}$ , in Figure 4. The agreement between the activation free energies from the model and the DFT calculations is reasonable (Figure 4A). Because the DFT activation free energies were previously shown to agree well with experiment,<sup>11c</sup> it is not surprising that the calculated and experimental activation energies are also in good agreement (Figure 4B). The calculated activation energies are smaller than experiment by  $\sim 1$  kcal/mol, mainly because the DFT activation free energies were smaller than the experimental values by the same amount.

In addition to the activation free energies, the model reproduces the other important features of the reaction. In general, the reactions are more exothermic and faster with electron donating groups and less exothermic and slower with electron withdrawing and delocalizing groups. These trends are expected on the basis of simple thermodynamic cycle arguments<sup>21</sup> and have been discussed in detail from a molecular structure perspective previously.<sup>11</sup> The model clearly illustrates the fundamental reason for these trends. An electron donating (or withdrawing group) raises (or lowers) the electronic energies of configurations in which the unpaired electron of the radical is in a  $\pi^*$  orbital more than when it is in a  $\sigma^*$  or nonbonding orbital on nitrogen. Thus, the energy of the  $\pi^*$  adiabat is raised by an electron donating group and lowered by a withdrawing group, whereas the  $\sigma^*$  adiabat is hardly changed. Thus, a donating group raises the energy of the attractive Morse curve in Figure 1 (the energies of the  $\pi^*$  and  $n\pi^*$  states are both raised) relative to the repulsive curve (the energies of the  $\sigma^*$  and  $n^2$  states are hardly changed), which results in a larger reaction exothermicity, earlier transition state, and faster reaction.

At the geometries corresponding to the bound radicals before fragmentation, the energy minima from the DFT calculations occur for values of  $r_{\text{N-O}}$  and  $\alpha$  ranging from 1.44 to 1.41 Å



**Figure 5.** (A) Out-of-plane bending angle,  $\alpha$ , at the bound radical minimum (closed circles) and transition state (open circles) and (B) N–O bond lengths,  $r_{\text{N-O}}$ , for (closed circles) the bound minimum and (open circles) the transition state, for fragmentation of *N*-methoxyppyridyl radicals, as a function of reaction exothermicity,  $E_{\text{rxn}}$ , predicted using the curve-crossing model described by eqs 2–6 and the parameters in Tables 1 and 2.

and 180 to 144°, respectively. The model allows lengthening and bending of the N–O bond at these minima as a result of mixing of the  $\pi^*$  and  $\sigma^*$  states. Mixing lowers the energy (in reality by allowing the electrons to occupy an orbital with considerable N–O  $\sigma^*$  character) as a result of eqs 3 and 4. The calculated radical minimum energy geometries are determined by balancing the energy increasing and decreasing factors, just as in the actual radicals. The extent to which state mixing occurs is determined by how close the diabats are in energy at any particular value of  $r_{\text{N-O}}$ . In the model, this is varied for the different reactions via the exothermicity parameter,  $E_{\text{rxn}}$ . The reactions with larger exothermicities bring the diabats closer together, which increases mixing, thus lowering the energy around the minimum geometry and lengthening and bending the bonds. The absolute values of the angles and bond lengths at the minima and the bond lengths at the transition states from the model compare reasonably well with those from the DFT (Table 3). The bond lengths at the minima are also reproduced reasonably well; however, as discussed above, the transition state angles are too large (Table 3). Nevertheless, the simple model apparently contains all of the essential features of the entire reaction surface.

The model predicts smooth increases in the length of the N–O bond and also the extent of bending at the bound minimum with increasing exothermicity (Figure 5). The N–O bond length and the bending angle both decrease at the transition state with increasing exothermicity, although the effect is much smaller than that for the minimum (Figure 5). Thus, the structures of the radical minima and transition states approach each other (the reactant radical increasingly approaches the structure of the transition state) with increasing exothermicity. The obvious limit in this regard is radical 7, in which the minimum and transition state have merged and for which DFT computations and experiment indicate that there is essentially no barrier at all.<sup>11</sup> This reaction is also predicted to be barrierless by the model, as clearly indicated in Figure 3.

Evidence in favor of barrierless solution phase electron transfer induced dissociation reactions has been sought for some time.<sup>17</sup> One-electron reduction of an appropriate aliphatic compound can form a three-electron  $\sigma$  bond (a  $\sigma^*$  radical) that is repulsive with respect to dissociation of that bond. Alkyl halides represent a classic example of this, and one-electron reduction to form the radical anion of many alkyl halides results in dissociation of the carbon–halogen bond without any barrier.<sup>18</sup> For organic systems containing an aromatic group, however, the lowest energy unoccupied orbital will in general

be a  $\pi^*$  orbital. As discussed above,  $\pi^*$  radicals are stable with respect to bond breaking, and  $\sigma^*$  character is required for reaction, which in turn requires curve crossing. Thus, it could be concluded that the dissociation of an aromatic radical anion will always have a barrier. However, the curve-crossing scheme discussed here nicely illustrates how the activation energy for fragmentation is decreased both by increasing the exothermicity and by increasing the splitting between the  $\pi^*$  and  $\sigma^*$  diabatic states. For the current case of radical **7**, a nominal reaction exothermicity of  $\sim 1$  eV and a state splitting also of  $\sim 1$  eV combine to the extent that the barrier to reaction completely disappears.

The simple quantitative curve-crossing model described here accurately describes the N–O bond fragmentation reaction in *N*-methoxypyridyl radicals and illustrates the molecular features required for barrierless reaction. One obvious extension of this work is a parametrization of the model without the need for the computations so that reaction rate constants could be predicted. Another is to apply the model to related reactions. Work along both lines is ongoing.

## Experimental Section

The DFT energy surfaces, radical minima, and transition state structures used in the simulations were those described in ref 11c. The time-dependent DFT computations were executed using the Gaussian 03 suite of programs.<sup>22</sup> The UB3PW91 method<sup>23</sup> was used with the 6-31G basis set<sup>24</sup> augmented with a set of Cartesian d orbitals on the second (and higher) period elements (polarization orbitals; 6-31G\*) and one set of diffuse orbitals<sup>25</sup> (6-31+G). The excitation energies of the planar *N*-methoxypyridyl radical were obtained by first completing a constrained optimization of the radical (N–O bond length of 1.40 Å,  $\alpha$  angle of 180.0°) using UB3PW91/6-31+G\*. This structure was then used for the TD DFT computation<sup>26</sup> [UB3PW91 TD(50-50,NStates=6)/6-31+G\*]. The orbitals were characterized visually using GaussView 3.0.<sup>27</sup>

**Acknowledgment.** A research grant from The Research Corporation is gratefully acknowledged. We thank J. T. Hynes (University of Colorado, Boulder) for preprints of his work on the related fragmentation reaction in the radical anion of *p*-cyanophenyl chloride.<sup>10</sup>

**Supporting Information Available:** Table S1 and Figure S1 illustrating the effect on the variable parameters of allowing the repulsive and Morse curves of Figure 1 to have different energy magnitudes and Table S2 comparing model and DFT electronic activation energies. This material is available free of charge via the Internet at <http://pubs.acs.org>.

## References and Notes

- (1) Eyring, H. *J. Chem. Phys.* **1934**, *3*, 107.
- (2) Moore, J. W.; Pearson, R. G. *Kinetics and Mechanism*, 3rd ed.; Wiley: New York, 1981.
- (3) (a) Bell, R. P. *Proc. R. Soc. London, Ser. A* **1936**, *154*, 414. (b) Evans, M. G.; Polanyi, M. *J. Chem. Soc., Faraday Trans.* **1936**, *32*, 1340.
- (4) Hammond, G. S. *J. Am. Chem. Soc.* **1955**, *77*, 334.
- (5) Marcus, R. A. *J. Phys. Chem.* **1968**, *72*, 891.
- (6) (a) Shaik, S. S. *J. Am. Chem. Soc.* **1981**, *103*, 3692. (b) Pross, A. *Theoretical Physical Principles of Organic Reactivity*; Wiley: New York, 1995. (c) Shaik, S.; Shurki, A. *Angew. Chem., Int. Ed. Engl.* **1999**, *38*, 586.
- (7) See, for example: (a) Andrieux, C. P.; Merz, A.; Saveant J.-M. *J. Am. Chem. Soc.* **1985**, *107*, 6097. (b) Constantin, C.; Hapiot, P.; Medebielle, M.; Saveant, J.-M. *J. Am. Chem. Soc.* **1999**, *121*, 4451. (c) Pause, L.; Robert, M.; Saveant, J.-M. *J. Am. Chem. Soc.* **1999**, *121*, 7158. (d) Constantin, C.; Robert, M.; Saveant, J.-M. *J. Phys. Chem. A* **2000**, *104*, 7492.
- (8) (a) Perhaps the best example of simulations of reaction rates comes from the extensive work of Saveant et al. on the fragmentation reactions of halide radical anions. See, for example: (b) Saveant, J.-M. *Adv. Electron Transfer Chem.* **1994**, *4*, 53.
- (9) For an example in electron transfer theory, see: Gould, I. R.; Noukakis, D.; Gomez-Jahn, L.; Young, R. H.; Goodman, J. L.; Farid, S. *Chem. Phys.* **1993**, *176*, 439.
- (10) (a) Laage, D.; Burghardt, I.; Sommerfeld, T.; Hynes, J. T. *ChemPhysChem* **2003**, *4*, 61. (b) Laage, D.; Burghardt, I.; Sommerfeld, T.; Hynes, J. T. *J. Phys. Chem. A* **2003**, *107*, 11271. (c) Burghardt, I.; Laage, D.; Hynes, J. T. *J. Phys. Chem. A* **2003**, *107*, 11292.
- (11) (a) Lorance, E. D.; Kramer, W. H.; Gould, I. R. *J. Am. Chem. Soc.* **2002**, *124*, 15225. (b) Lorance, E. D.; Kramer, W. H.; Gould, I. R. *J. Am. Chem. Soc.* **2004**, *126*, 14071. (c) Lorance, E. D.; Hendrickson, K.; Gould, I. R. *J. Org. Chem.*, in press.
- (12) See, for example: (a) Zimmerman, H. E. *J. Am. Chem. Soc.* **1966**, *88*, 1566. (b) Michl, J. *J. Mol. Photochem.* **1972**, *243*. (c) Klessinger, M. *J. Photochem. Photobiol., A* **2001**, *144*, 217.
- (13) See, for example: (a) Blancfort, L.; Jolibois, F.; Olivucci, M.; Robb, M. A. *J. Am. Chem. Soc.* **2001**, *123*, 722. (b) Bearpark, M. J.; Robb, M. A.; Yamamoto, N. *Spectrochim. Acta, Part A* **1999**, *55*, 639. (c) Blancfort, L.; Adam, W.; Gonzalez, D.; Olivucci, M.; Vreven, T.; Robb, M. A. *J. Am. Chem. Soc.* **1999**, *121*, 10583. (d) Diau, E. W.-G.; De Feyter, S.; Zewail, A. H. *Chem. Phys. Lett.* **1999**, *304*, 134.
- (14) Newton, M. D. In *Electron Transfer in Chemistry*; Balzani, V., Ed.; Wiley-VCH: New York, 2001; Vol. 1, p 3.
- (15) (a) Butler, L. *J. Annu. Rev. Phys. Chem.* **1998**, *49*, 125. (b) Piotrowiak, P. In *Electron Transfer in Chemistry*; Balzani, V., Ed.; Wiley-VCH: New York, 2001; Vol. 1, p 215.
- (16) For a recent example, see: Gould, I. R.; Lenhard, J.; Farid, S. *J. Phys. Chem. A* **2004**, *108*, 10949.
- (17) See, for example: (a) Maslak, P.; Kula, J.; Chateaufort, J. E. *J. Am. Chem. Soc.* **1991**, *113*, 2304. (b) Bockman, T. M.; Lee, K. Y.; Kochi, J. K. *J. Chem. Soc., Perkin Trans. 2* **1992**, 1581. (c) Bockman, T.; Hubig, M. S.; Kochi, J. K. *J. Am. Chem. Soc.* **1998**, *120*, 6542. (d) Rasmusson, M.; Akesson, E.; Ebersson, L.; Sundstrom, V. *J. Phys. Chem. B* **2001**, *105*, 2027. (e) Schmittel, M.; Ghorai, M. K. In *Electron Transfer in Chemistry*; Balzani, V., Ed.; Wiley-VCH: New York, 2001; Vol. 2, p 18.
- (18) See, for example: ref 6b, pp 93, 94, 247, and 248.
- (19) Jensen, F. *Introduction to Computational Chemistry*; Wiley: New York, 1999; p 11.
- (20) The electronic activation energies from the model,  $\Delta E^{\ddagger}_{\text{calcd}}$ , are compared to the corresponding DFT electronic activation energies,  $\Delta E^{\ddagger}_{\text{DFT}}$ , in the Supporting Information.
- (21) (a) Popielarz, R.; Arnold, D. R. *J. Am. Chem. Soc.* **1990**, *112*, 3068. (b) Maslak, P.; Vallombroso, T. M.; Chapman, W. H., Jr.; Narvaez, J. N. *Angew. Chem., Int. Ed. Engl.* **1994**, *33*, 73. (c) Gaillard, E. R.; Whitten, D. G. *Acc. Chem. Res.* **1996**, *29*, 292.
- (22) Frisch, M. J.; Trucks, G. W.; Schlegel, H. B.; Scuseria, G. E.; Robb, M. A.; Cheeseman, J. R.; Montgomery, J. A., Jr.; Vreven, T.; Kudin, K. N.; Burant, J. C.; Millam, J. M.; Iyengar, S. S.; Tomasi, J.; Barone, V.; Mennucci, B.; Cossi, M.; Scalmani, G.; Rega, N.; Petersson, G. A.; Nakatsuji, H.; Hada, M.; Ehara, M.; Toyota, K.; Fukuda, R.; Hasegawa, J.; Ishida, M.; Nakajima, T.; Honda, Y.; Kitao, O.; Nakai, H.; Klene, M.; Li, X.; Knox, J. E.; Hratchian, H. P.; Cross, J. B.; Bakken, V.; Adamo, C.; Jaramillo, J.; Gomperts, R.; Stratmann, R. E.; Yazyev, O.; Austin, A. J.; Cammi, R.; Pomelli, C.; Ochterski, J. W.; Ayala, P. Y.; Morokuma, K.; Voth, G. A.; Salvador, P.; Dannenberg, J. J.; Zakrzewski, V. G.; Dapprich, S.; Daniels, A. D.; Strain, M. C.; Farkas, O.; Malick, D. K.; Rabuck, A. D.; Raghavachari, K.; Foresman, J. B.; Ortiz, J. V.; Cui, Q.; Baboul, A. G.; Clifford, S.; Cioslowski, J.; Stefanov, B. B.; Liu, G.; Liashenko, G.; Piskorz, P.; Komaromi, I.; Martin, R. L.; Fox, D. J.; Keith, T.; Al-Laham, M. A.; Peng, C. Y.; Nanayakkara, A.; Challacombe, M.; Gill, P. M. W.; Johnson, B.; Chen, W.; Wong, M. W.; Gonzalez, C.; Pople, J. A. *Gaussian 03*, revision C.02; Gaussian, Inc.: Wallingford, CT, 2004.
- (23) (a) Becke, A. D. *J. Chem. Phys.* **1993**, *98*, 5648. (b) Burke, K.; Perdew, J. P.; Wang, Y. In *Electronic Density Functional Theory: Recent Progress and New Directions*; Dobson, J. F., Vignale, G., Das, M. P., Eds.; Plenum: New York, 1998. (c) Perdew, J. P. In *Electronic Structure of Solids '91*; Ziesche, P., Eschrig, H., Eds.; Akademie Verlag: Berlin, 1991; p 11. (d) Perdew, J. P.; Chevary, J. A.; Vosko, S. H.; Jackson, K. A.; Pederson, M. R.; Singh, D. J.; Fiolhais, C. *Phys. Rev. B* **1992**, *46*, 6671. (e) Perdew, J. P.; Chevary, J. A.; Vosko, S. H.; Jackson, K. A.; Pederson, M. R.; Singh, D. J.; Fiolhais, C. *Phys. Rev. B* **1993**, *48*, 4978. (f) Perdew, J. P.; Burke, K.; Wang, Y. *Phys. Rev. B* **1996**, *54*, 16533.
- (24) Ditchfield, R.; Hehre, W. J.; Pople, J. A. *J. Chem. Phys.* **1971**, *54*, 724. Hehre, W. J.; Ditchfield, R.; Pople, J. A. *J. Chem. Phys.* **1972**, *56*, 2257. Hariharan, P. C.; Pople, J. A. *Mol. Phys.* **1974**, *27*, 209. Gordon, M. S. *Chem. Phys. Lett.* **1980**, *76*, 163. Hariharan, P. C.; Pople, J. A. *Theor. Chim. Acta* **1973**, *28*, 213. Blaudeau, J.-P.; McGrath, M. P.; Curtiss, L. A.;

Radom, L. *J. Chem. Phys.* **1997**, *107*, 5016. Francl, M. M.; Pietro, W. J.; Hehre, W. J.; Binkley, J. S.; DeFrees, D. J.; Pople, J. A.; Gordon, M. S. *J. Chem. Phys.* **1982**, *77*, 3654. Binning, R. C., Jr.; Curtiss, L. A. *J. Comput. Chem.* **1990**, *11*, 1206. Rassolov, V. A.; Pople, J. A.; Ratner, M. A.; Windus, T. L. *J. Chem. Phys.* **1998**, *109*, 1223. Rassolov, V. A.; Ratner, M. A.; Pople, J. A.; Redfern, P. C.; Curtiss, L. A. *J. Comput. Chem.* **2001**, *22*, 976.

(25) Clark, T.; Chandrasekhar, J.; Spitznagel, G. W.; Schleyer, P. v. R. *J. Comput. Chem.* **1983**, *4*, 294.

(26) (a) Bauernschmitt, R.; Ahlrichs, R. *Chem. Phys. Lett.* **1996**, 256, 454. Casida, M. E.; Jamorski, C.; Casida, K. C.; Salahub, D. R. *J. Chem. Phys.* **1998**, *108*, 4439. Stratmann, R. E.; Scuseria, G. E.; Frisch, M. J. *J. Chem. Phys.* **1998**, *109*, 8218.

(27) *GaussView 3.0*; Gaussian, Inc.: Wallingford, CT, 2002–2003.